Published in IET Microwaves, Antennas & Propagation
Received on 30th November 2009
Revised on 4th March 2010
doi: 10.1049/iet-map.2009.0593

In Special Issue on Microwave Metamaterials: Application to Devices, Circuits and Antennas

ISSN 1751-8725

Electromagnetic bandgap filter with single-cell monolithic microwave integrated circuit-tuneable defect

K. Herbertz S. Lucyszyn

Department of Electrical and Electronic Engineering, Imperial College London, London SW7 2AZ, UK
E-mail: k.herbertz@imperial.ac.uk

Abstract: A prototype tuneable planar electromagnetic bandgap filter has been developed for implementing a voltage-controlled bandwidth, intended for adaptive spectral control. A tuneable single-cell defect that allows tuning of the bandwidth is introduced into the structure using monolithic microwave integrated circuit technology. A combination of three-dimensional electromagnetic modelling of the planar structure and equivalent circuit modelling techniques is presented to validate this work. The simulation and measured results are in very close agreement.

1 Introduction

In recent years, efforts have been made to create standards for cognitive radio and dynamic spectrum access [1]. Economic models on the aspect of spectrum trading in cognitive radio networks have been investigated [2], which suggests that the importance of cognitive radio networks is going to increase. For applications that require dynamic spectrum access, filters with a tuneable bandwidth are needed. With conventional filter technologies, this can be achieved with the use of multiple tuning elements. However, this approach may not be simple in practice. An alternative approach is adopted here, using a planar electromagnetic bandgap (EBG) filter, with an integrated tuneable cell defect.

The term 'metamaterials' encompasses various periodic structures with properties that do not exist in nature. There are several different classes of metamaterials. Engheta and Ziolkowski divided their book on metamaterials into the single- and double-negative material class and the EBG-structured metamaterial class [3]. Although frequency selective surfaces (FSSs), EBGs and metamaterials are all periodic structures, the period p of metamaterials is significantly smaller than the guided wavelength λ_g [4]. The period for EBGs is of the order of half a guided wavelength: $p \sim \lambda_g/2$ [4]. As their names suggest, an EBG exhibits a specific frequency characteristic in its transmittance and/or reflectance properties, whereas the more general FSSs may also alter other aspects such as polarity or group delay.

EBG structures derive their name from an analogy to solid-state electronic bandgap structures. With the latter, there are certain energy bands that electrons can occupy and forbidden bands that cannot be occupied. With EBGs, the forbidden bands pertain to energy levels that photons cannot occupy. Hence, electromagnetic (EM) waves with a frequency inside the forbidden band cannot propagate through the EBG material, irrespective of their angle of incidence [5].

EBGs were first reported for structures at optical wavelengths in 1987 [6]. Over the intervening years, artificial structures have been engineered at much longer wavelengths.

Planar EBGs are of particular interest at microwave frequencies, because of their ease of fabrication. These EBGs are usually only periodic in a two-dimensional (2D) plane and do not exhibit a bandgap for all angles of incidence of an EM wave, but just for all angles in one plane. Within the group of planar EBGs, the uniplanar compact (UC) EBG [7] was adopted for its simplicity.

In order to improve the functionality of EBG and metamaterial structures, their properties can be made

tuneable. Typically, the tuning approach consists of changing the inductive or capacitive properties of the structure and, thus, the frequency of resonance for individual cells. Several methods for tuning EBGs and metamaterials have been proposed in the literature; for example, capacitive elements are tuned by exploiting the temperature dependence of the associated dielectric constant of ferroelectric thin films [8]. A large number of publications describe methods of tuning the capacitance by adding varactors [9]; this appears to be the most common method of tuning. For instance, ferroelectric varactors have been used to tune the behaviour of left-handed phase shifters [10]. Instead of tuning the capacitance, an equivalent approach is to use tuneable active inductors [11]. Moreover, a double-negative material was built with magnetodielectric spherical particles and their properties were tuned with a magnetic field of varying strength [12]. Switching between two states is another method of implementing tuneability, which was realised with microelectromechanical system (MEMS) switches on split-ring resonators (SRRs) [13]. Optical control, that is, illumination of semiconductors to generate electron–hole pair free carriers, has also been used to tune SRRs [14]. Alternatively, PIN diodes can also be used within an FSS, to control the operating frequency of an EBG resonator antenna [15]. Finally, liquid crystals have been employed to tune FSSs [16].

This paper describes a special case of varactor tuning for an EBG filter by employing be-spoke monolithic microwave integrated circuits (MMICs). The following section describes the EBG cell and the differences between the conventional and the modified UC-EBGs. Section 3 presents a prototype printed circuit board (PCB) EBG filter. Simulation and measurement results are shown for the un-tuned filter. An equivalent circuit model was created to evaluate the effect of introducing a tuneable cell defect. MMICs, having integrated varactors and associated biasing, are introduced and then applied to realise a filter having a single-cell tuneable defect. Section 4 discusses the comparison between the simulated and measured EBG filter responses, as well as the implementation of a monolithic EBG structure on a fused silica wafer. Finally, Section 5 draws conclusions from this work.

2 EBG cell

The conventional UC-EBG cell in microstrip has a shunt capacitance of C_p and is coupled to one of four adjacent cells by a series inductance L_s in parallel with two series capacitances C_s. Fig. 1*a* illustrates the conventional UC-EBG cell.

Two technologies for realising a UC-EBG cell are presented in this paper; one using low-cost PCB and the other micromachined on a fused silica wafer. Table 1 summarises the dimensions for the PCB and monolithic designs. The dimensions are specified as multipliers of cell size a. For the PCB design the cell size $a = 10$ mm, and for the wafer design the cell size $a = 1$ mm.

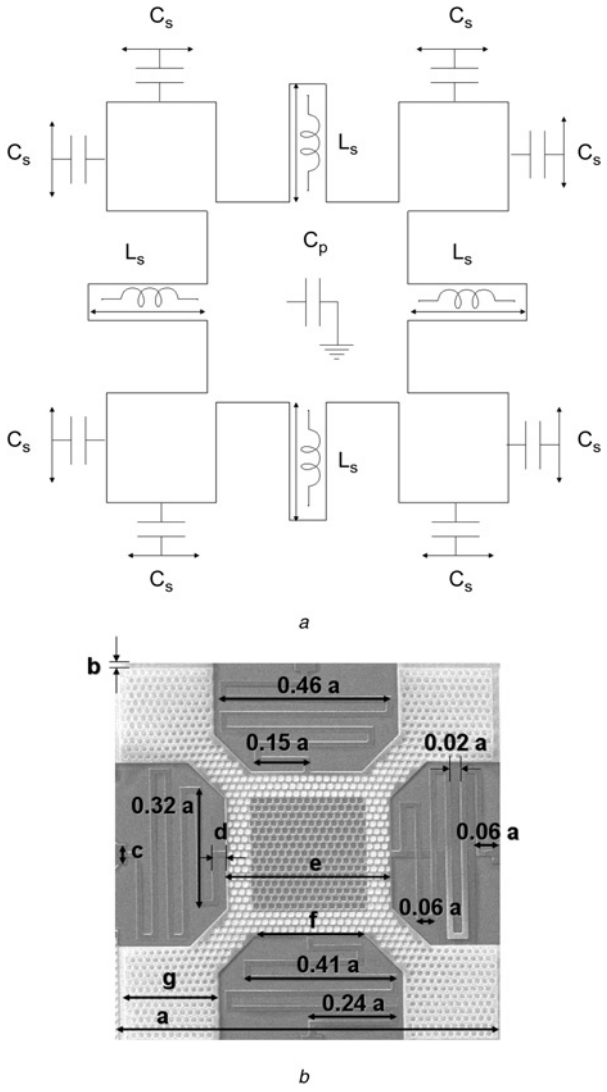

Figure 1 *UC-EBG cell and its modification*
a Plan view of the conventional UC-EBG cell
b SEM image of a micromachined modified UC-EBG cell

Fig. 1*b* shows a scanning electron microscope (SEM) photograph of a modified UC-EBG cell. It can be seen

Table 1 Dimensions for the PCB and monolithic cell

Dimension	PCB	Monolithic
a	10 mm	1 mm
b	0.01 × *a* (100 μm)	0.005 × *a* (5 μm)
c	0.02 × *a* (200 μm)	0.06 × *a* (60 μm)
d	0.045 × *a* (450 μm)	0.04 × *a* (40 μm)
e	0.43 × *a* (4.3 mm)	0.44 × *a* (440 μm)
f	0.31 × *a* (3.1 mm)	0.29 × *a* (290 μm)
g	0.24 × *a* (2.4 mm)	0.25 × *a* (250 μm)

doi: 10.1049/iet-map.2009.0593

that the inductances have been increased by changing their associated geometry from a short straight wide line to a long meandered thin line. At the end of each meander, at the border to the adjacent cell, there is an anchor point. With the PCB version, the cells are not suspended and the anchor points are vias down to ground. This solution provides shunt inductance to the cell, while effectively removing the series inductive coupling between cells. With the monolithic version, shown in Fig. 1*b*, the anchor points are attached to the substrate and provide the only mechanical supports for its cell, in order to allow the cell to be suspended above the wafer. This advanced solution, briefly introduced here, allows independent RF MEMS tuning of the shunt capacitance for each individual cell; therefore the meandered inductance lines also act as mechanical springs.

Historically, the theory for wave propagation in periodic structures was solved analytically for simple periodic structures [17]. Today, the bandgap of even complex structures can be obtained by numerical means. To verify that the examined EBG structure exhibits a bandgap, the theoretical dispersion diagram was computed with the eigenmode solver within the Ansoft High Frequency Structure Simulator (HFSS^{TM}) software. The solution set-up for the finite element method-based bandgap analysis has been previously described [18].

In order to simulate an infinite array, one unit cell (encapsulated by an air box) is modelled and periodic boundaries are set up along its sides. On top of the air box is a perfectly matched layer, which is terminated by a perfect electric conductor. In a noteworthy paper [19], Coccioli *et al.* characterised a planar UC-EBG, which included dispersion diagrams. They used the field distribution to identify the nature of the modes. Because of the nature of the modified UC-EBG cell, it is difficult to isolate one particular mode. For instance, with the second mode, neither the electric nor magnetic field vectors are transversal to the direction of propagation.

Fig. 2 shows the dispersion diagram for the PCB's modified UC-EBG cell, constructed using data points extracted from HFSS^{TM}. Although the branches from Γ to X and X to M are equidistant, the branch from M to Γ is longer. Consequently, the spacing between points increase in the M to Γ branch, as it contains the same amount of data points as the other branches. Fig. 2 shows the first and third modes, which have been identified as being TM in nature, from which the corresponding bandgap can be seen.

In HFSS^{TM} the eigenmode solver determines the complex resonant mode frequency of a structure $\tilde{\omega}_0$ [20]. The solid points in Fig. 2 have an unloaded quality (Qu)-factor > 59, with the exception of the point at 45° in the M to Γ branch, which has a Qu = 5.4. The hollow points have a Qu < 5. For each resonant mode frequency, the unloaded

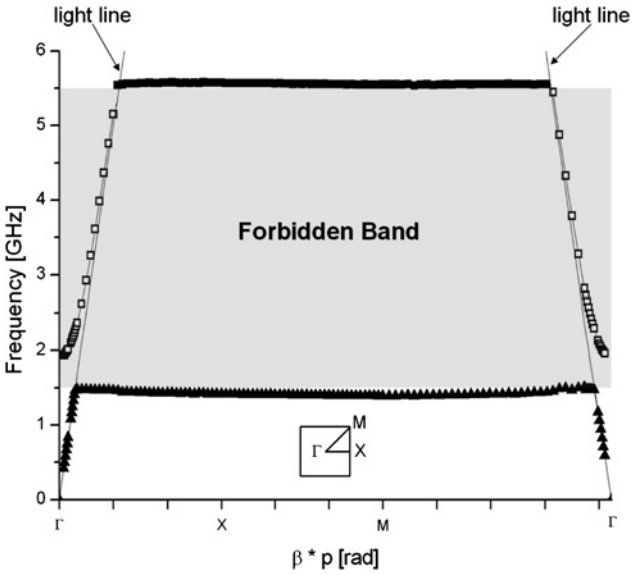

Figure 2 *Dispersion diagram for the PCB's modified UC-EBG cell, extracted using HFSS^{TM} with tan δ = 0.0018*

Qu-factor can be calculated as follows [20]:

$$Qu(|\tilde{\omega}_0|) = \frac{1}{2}\sqrt{\left(\frac{\Re\{\tilde{\omega}_0\}}{\Im\{\tilde{\omega}_0\}}\right)^2 + 1} \quad (1)$$

where $\Re\{\}$ and $\Im\{\}$ represent the real and imaginary parts, respectively, of the bracketed term. A low Qu-factor indicates high attenuation of the corresponding propagating mode. If these modes are sufficiently attenuated, the EM waves are quasi-evanescent and, thus, those frequency points can be ignored when determining the bandgap. This is the case when the real part is less than 10 times the imaginary part of the resonant frequency [18]. In terms of the unloaded Qu-factor, this cut-off point corresponds to Qu = 5.0, according to (1). For this reason, in Fig. 2, the grey area in between the two TM modes denotes the forbidden band, which lies between 1.5 and 5.5 GHz.

3 EBG filter

The generic layout of the EBG filter is illustrated in Fig. 3*a*. It consists of a central through transmission line with two symmetrical 2D EBG $X \times Y$ arrays on either side. At the periphery of each array, the cells are coupled to either the transmission line or ground strip via the cell's series inductance. For frequencies within the forbidden band of the EBG array, the array constitutes a high impedance path to ground. Therefore, EM waves at those frequencies are propagating along the transmission through line with little attenuation. At other frequencies, the array provides a low impedance path to ground, thus acting as a filter by preventing propagation along the transmission through line. It will be shown that a single defective cell can be introduced to provide tuneability to the filter.

3.1 Non-tuneable filter

Non-tuneable EBG filters have been previously designed with the cell structure described in Section 2 [21]. A 250 μm thick Taconic RF35 substrate (having a dielectric constant $\varepsilon_r = 3.5$ and loss tangent $\tan\delta = 0.0018$ at 1.9 GHz) was used for the prototype filter. The copper layers are 18 μm thick, coated with a very thin layer of gold to prevent oxidisation of the copper.

Fig. 3*b* shows the predicted and measured performances for the PCB version of the modified UC-EBG cell array filter. A 3D electromagnetic model of the proposed structure was simulated using HFSS^{TM}. The dashed lines in Fig. 3*b* denote the HFSS^{TM} simulation results. Initially, the HFSS^{TM} simulation exhibited a discrepancy of about 2 dB in insertion loss when compared to the measurements. This discrepancy could be attributed to either the conductor or substrate. Further simulations with lower conductivity values could not explain this discrepancy. However, it could be explained with a value of $\tan\delta = 0.04$ for the dielectric loss tangent of the substrate. In addition to 3D electromagnetic modelling, the structure was also modelled using a 2D circuit simulator with Microwave Office. The 2D equivalent circuit model for a 4×1 cell array was based on the previously constructed 3×1 model [21]. By adding one additional column of cells, the response of the 4×1 filter could be predicted. The dotted lines denote the equivalent circuit simulation results. The predicted 2D modelling results are in good agreement with the measurements. This confirmed the versatility and accuracy of this modelling approach. The solid lines denote the measurement results. It can be seen that the measured results are in good agreement with the predictions for both the rigid 3D electromagnetic and versatile 2D equivalent circuit modelling approaches.

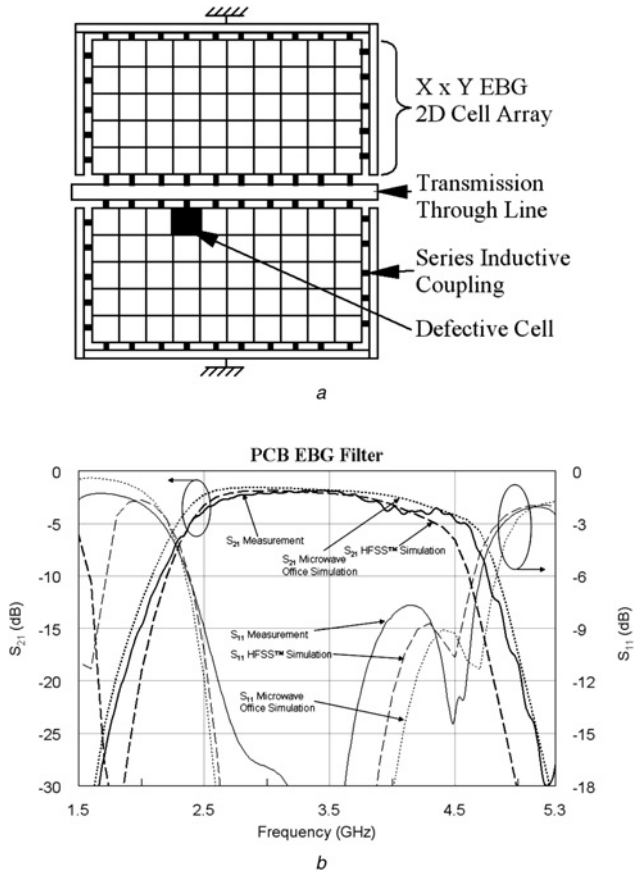

Figure 3 *EBG filter*

a Generic layout
b Predicted and measured performances for the PCB version of the modified UC-EBG cell array filter

3.2 Monolithic microwave integrated circuits

With the transmission through line, EBG arrays and ground bars electrically connected at direct current (DC), it is not easy to bias varactors directly, since additional DC blocking capacitors would be needed. Moreover, the sizes of the bias components may be comparable to the individual cells, which present a range of practical implementation issues. Therefore, in order to avoid undue complexity, a unique solution had to be found. To this end, MMICs were introduced; their be-spoke designs have integrated varactor diodes and associated bias circuitry. The design of the MMIC can be seen in Fig. 4*a*, whereas the corresponding microphotograph of the chip can be seen in Fig. 4*b*. The MMIC can be easily bonded directly onto a cell, using conductive epoxy glue, and then wire-bonded to the transmission line of the filter; thereby providing additional and tuneable series capacitance between the 'defective' cell and the transmission line.

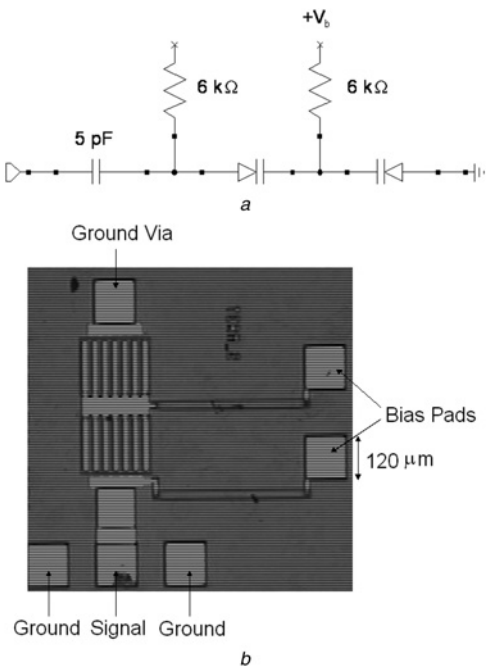

Figure 4 *MMIC pre-bonding*

a MMIC design
b Microphotograph of the realised MMIC

doi: 10.1049/iet-map.2009.0593

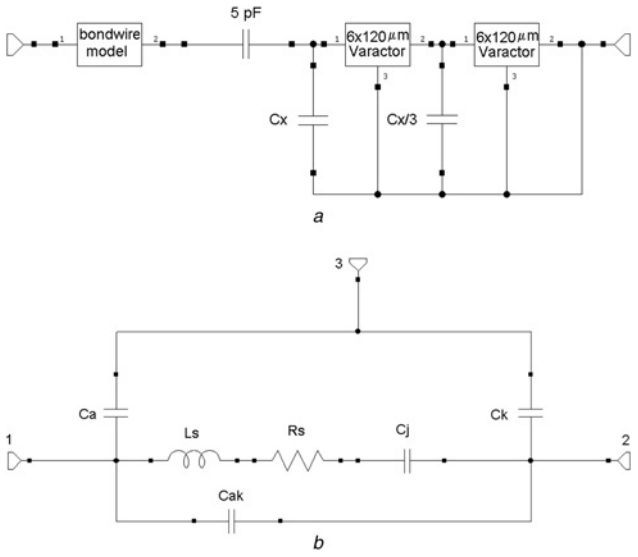

Figure 5 *Equivalent circuit models for the MMIC and varactors post-bonding*

a Equivalent circuit model for the complete MMIC
b Equivalent circuit model for the varactor

Table 2 MMIC equivalent circuit element values

Component	Scaled value	Adjusted value
Cx	0.02 pF	–
Ca	0.0008 pF	–
Cak	0.024 pF	–
Cj	0.924 pF	1.25 pF
Ck	0.008 pF	–
Ls	0.02 nH	0.2 nH
Rs	3 Ω	–

A hybrid approach was adopted for the overall 2D equivalent circuit model of the filter, whereby the defective cell was represented by an equivalent circuit model of the MMIC in conjunction with a 3-port 3D electromagnetic model for a non-defective cell. In addition, a bond wire model (consisting of a series inductor and resistor, having frequency-dependeant values) was also needed. Detailed equivalent circuit modelling of the MMIC had to be undertaken using information previously published [22–26]. The GaAs MMICs include two interdigitated planar Schottky varactor diodes (IPSVDs), each having a gate periphery of 6 × 120 μm [22], with the basic model being previously published [23, 24]. The element values were then scaled according to empirical results [24]. Fig. 5 gives the equivalent circuit model for the complete MMIC, with that for the individual IPSVD shown in Fig. 5*b*.

The ground plane of the MMIC can act as its own port terminal. As such, this one-port MMIC can be treated as a two-port component. Here, the one-port measurement (i.e. s1p) files of the MMIC were converted into two-port (i.e. s2p) files, by mapping the ground of the one-port file to a signal port in Agilent's Advanced Design System software. The MMIC's equivalent circuit model results are in good agreement with those of the two-port 'measurements'. Having said this, two of the scaled element values were tweaked to provide a better fit. Both the scaled values and the adjusted values are given in Table 2. The discrepancies between the scaled element values and those fitted to the measurements can be explained by the fact that the scaling laws only represent an approximation.

3.3 Tuneable cell defect filter

With the initial 2D equivalent circuit modelling approach, ideal tuneable capacitors were introduced, instead of the complete MMIC model, at different locations. The best results were obtained when the two variable capacitors were introduced between the transmission line and a connecting cell. Since the existing coupling capacitors between cells have a capacitance of ~2 fF, this series capacitive coupling between cells is negligible. As a result, the model can be further simplified to that depicted in Fig. 6.

The variables in Fig. 6 have the following values: length of the transmission line segments len1 = 3.7 mm,

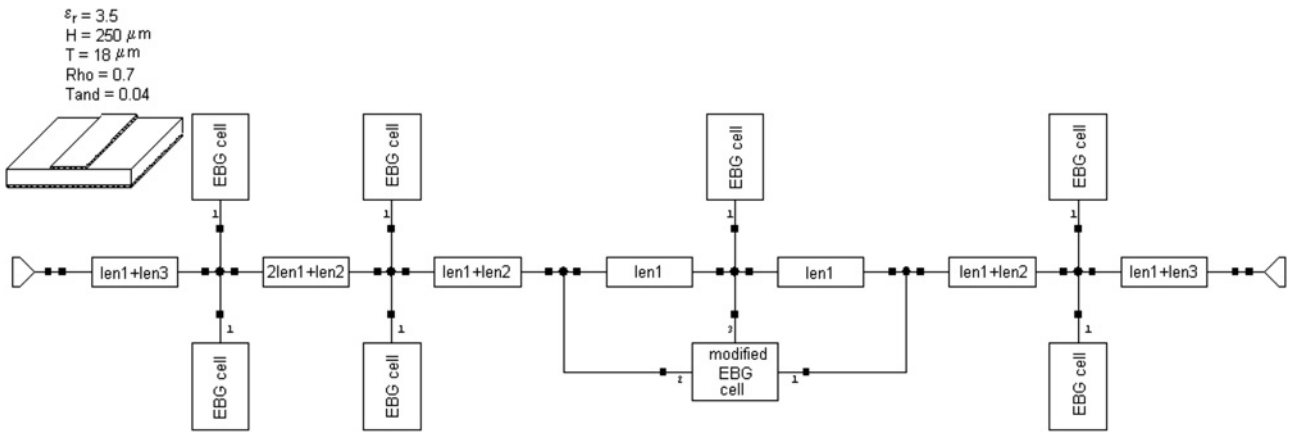

Figure 6 *Simplified hybrid 2D equivalent circuit model for the PCB version of the modified UC-EBG 4 × 1 cell array filter*

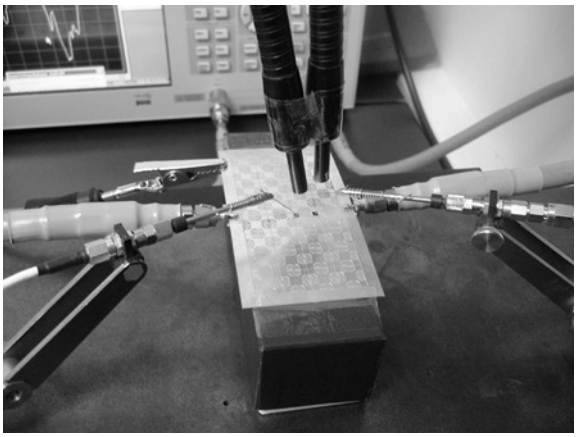

Figure 7 *A 4 × 4 cell array version of the modified UC-EBG filter under test*

len2 = 2.6 mm, len3 = 6.3 mm, resistivity of copper relative to that of gold Rho = 0.7 and effective (fitted) dielectric loss tangent tan δ = 0.04. The transmission line segments each have a width of 550 μm.

The EBG cells consist of a capacitance to ground of 5.6 pF and the four meandered inductors, three of which are grounded and one connects the cell to the transmission line. The meanders were modelled by transmission lines of 200 μm width and effective (fitted) length of 15.77 mm.

4 Filter performance

4.1 Prototype PCB

In order to implement a tuneable band-pass filter, two MMICs were placed in parallel with the series coupling

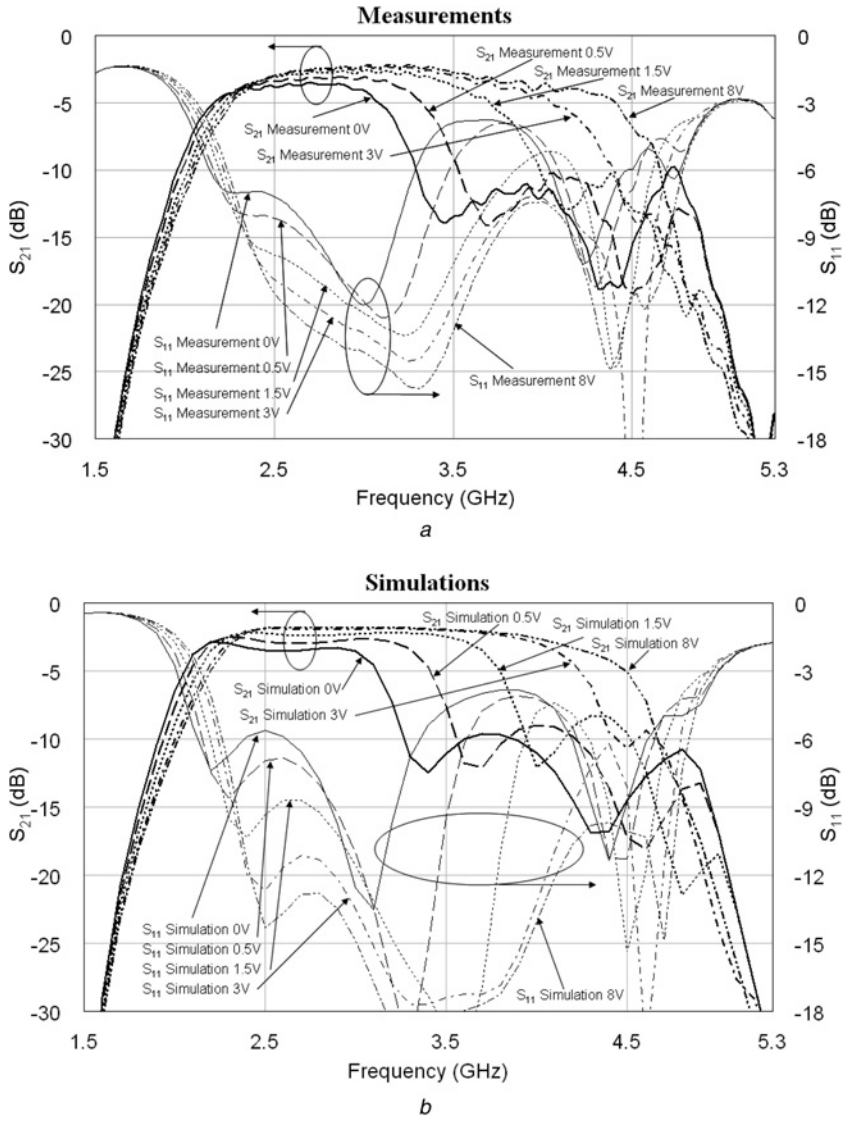

Figure 8 *Simulations and measurements of the tuneable single-cell defect PCB EBG filter*

a Measured filter behaviour at five different varactor bias voltages
b Simulated filter behaviour at the same five varactor bias voltages

doi: 10.1049/iet-map.2009.0593

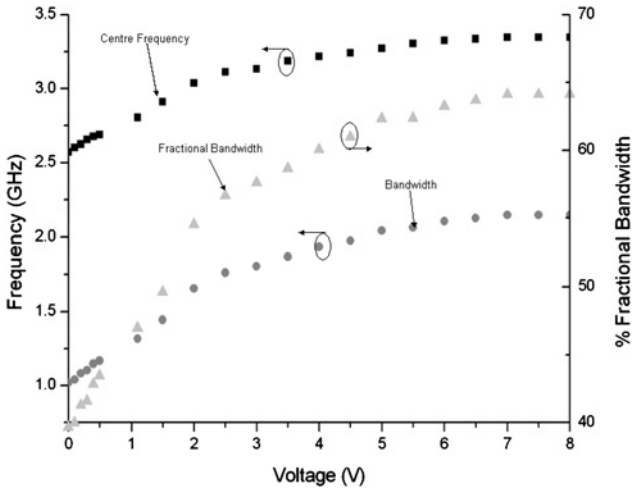

Figure 9 *Measured tuning behaviour for the centre frequency, 3 dB bandwidth and fractional bandwidth of the pass band*

capacitances between the transmission line and one adjacent cell. The MMICs were attached onto this cell using EPO-TEK® H20E-175 conductive epoxy glue. Bond wires also connect the MMIC to the transmission line.

Fig. 7 shows a 4 × 4 cell array version of the modified UC-EBG filter under test. For this prototype design, DC probe needles were attached to the MMICs in order to provide the bias voltage for the varactors.

Since the varactors within the MMIC have a much larger capacitance (~1 pF) than the previously omitted series coupling capacitances (~2 fF), the influence of this path can no longer be overlooked. Fig. 6 includes the two additional paths for the modified UC-EBG cell. Although the hybrid modelling approach can be further improved, an excellent match between measurement and simulations was achieved when the complete filter is modelled using only equivalent circuit modelling techniques. Fig. 8*a* gives the measurements and Fig. 8*b* the corresponding simulation results for the same variable values quoted for Fig. 6. Here, the results for five different varactor bias voltages (from 0 to 8 V) are presented, to demonstrate the 2:1 3 dB bandwidth tuneability of this filter. With increasing bias voltage, the junction capacitances of the IPSVDs decrease. Since the impedance increases with decreasing capacitance, the original state having negligible series coupling capacitance is achieved at 8 V.

Fig. 9 shows the measured tuning behaviour for the centre frequency, bandwidth and fractional bandwidth of the pass band. As expected, the centre frequency, fractional bandwidth and bandwidth increase with increasing IPSVD bias voltage.

4.2 Monolithic

Based on the results from the prototype PCB filter, a highly compact non-tuneable version was developed, using surface micromachining on a fused silica wafer, for operation at higher frequencies. With this new design, adjacent cells are now linked by both series capacitive and inductive coupling. As a result, the additional rows influence the behaviour of the structure. HFSS™ simulations have confirmed that the isolation in the upper stop band now increases with the number of rows.

The first monolithic prototype was fabricated by VTT Mililab (Finland). The bridge layer, which gives suspended structures, is made of 1.5 μm sputtered aluminium. The multi-metal (i.e. 50 nm TiW, 400 nm Au and 50 nm TiW) ground plane was approximated by a 500 nm gold layer within the HFSS™ simulations. Since bulk conductivity cannot be applied to thin films, approximately one-third of the conductivity was assumed for these simulations, to account for the higher sheet resistance of the thin films (1.2×10^7 S/m for the aluminium and 1.3×10^7 S/m for the gold layer).

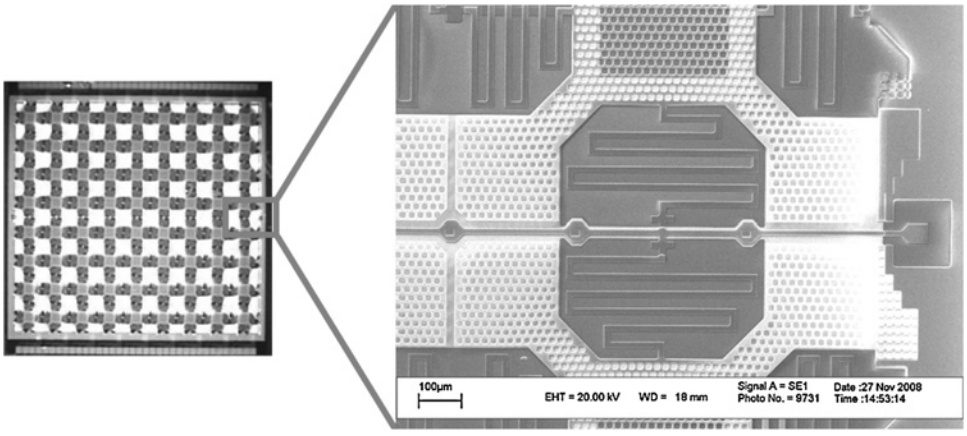

Figure 10 *Photograph of the complete monolithic filter and SEM micrograph of the output region of the through transmission line*

doi: 10.1049/iet-map.2009.0593

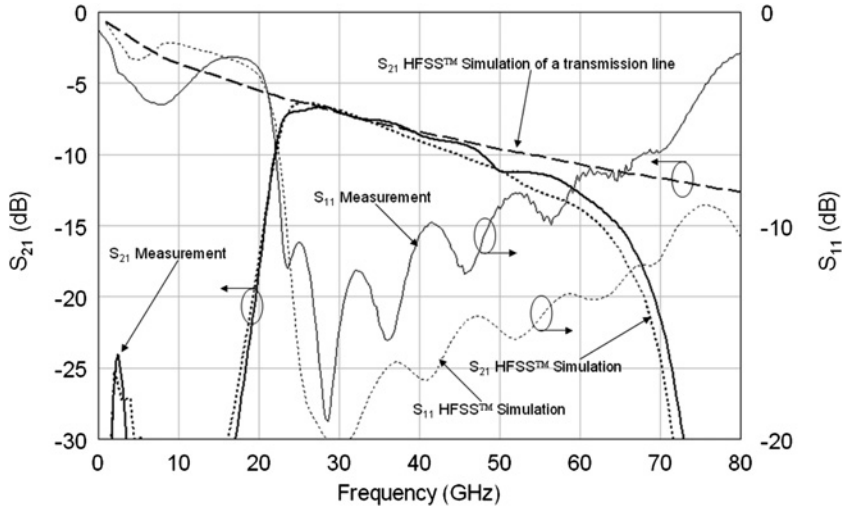

Figure 11 *Prediction and measurement results for the compact filter*

Fig. 10 shows the complete filter on the left-hand side and a magnification of the through transmission line on the right-hand side, with adjacent cells above and below this line. The complete area of the filter is only 1 cm^2, with the dimensions of each cell being 1×1 mm^2. Similar to the PCB filter, two modified UC-EBG cell arrays are connected to a central microstrip through transmission line. The size of the array has been expanded to 9×4 cells. Unlike the PCB version, the microstrip line and the EBG cells are suspended 2.3 μm above the wafer and connected to the fused silica substrate with electrically -isolated anchors.

Fig. 11 shows the insertion loss and return loss of both the predicted HFSS^{TM} simulations (dotted line) and measurement (solid line) of this new filter. It can be seen that the measured performance is in good agreement with that predicted. Also shown in Fig. 11, the predicted insertion loss performance (dashed line) of the suspended microstrip line is given, having the same material properties and dimensions as that for the filter. It can be clearly seen that the slope within the pass band of the filter is bounded by the insertion loss of the discrete transmission line.

Therefore, it can be deduced that the transmission line losses need to be reduced further, in order to be able to realise a more characteristic band-pass filter response. By introducing a tuneable cell defect, similar to the method shown for the prototype PCB filter, the bandwidth can be varied. Moreover, by transforming the normally fixed shunt capacitances of each cell into RF MEMS tuneable capacitances, the position of the lower pass band cut-off frequency can be controlled. Therefore, by combining both approaches a filter with complete pass band tuneability can be realiseized.

5 Conclusions

Prototype EBG filters implemented using low-cost PCB and advanced monolithic processing technologies have been designed, fabricated and measured. A bandwidth tuneability of 2:1 has been achieved with the PCB filter, by introducing a single-cell defect employing two MMICs. In addition to the 3D electromagnetic model of the filter, a comprehensive 2D equivalent circuit model was devised. Simulations have confirmed that the extent of the tuneability is not due to an increased coupling capacitance between the transmission line and the EBG cell, but due to the creation of additional signal paths and the distributed transmission line behaviour of the cell.

Following the initial work of the prototype monolithic filter, the next step is to introduce some form of tuneability. This could combine both single-cell defects and RF MEMS tuneable shunt capacitance in each cell. Tuning the latter would mainly influence the low-frequency behaviour of the pass band, due to its effect on the second transmission zero. With the additional tuning of the high-frequency behaviour of the pass band, provided by the single-cell defect, the complete pass band could be made tuneable.

6 Acknowledgments

This work is partly funded by the UK's Engineering and Physical Sciences Research Council (EPSRC), under the Platform Grant entitled 'Platform Support for 3D Electrical MEMS' (EP/E063500/1). It was also partly funded by the European Union's Network of Excellence on 'Advanced MEMS for RF and Millimeter Wave Communications (AMICOM)' (FP6-507352). The authors would like to thank Dr Oleksiy Sydoruk for the helpful discussions on mode identification.

7 References

[1] SHERMAN M., MODY A.N., MARTINEZ R., RODRIGUEZ C., REDDY R.: 'IEEE standards supporting cognitive radio and networks, dynamic spectrum access, and coexistence', *IEEE Commun. Mag.*, 2008, **46**, (7), pp. 72–79

doi: 10.1049/iet-map.2009.0593

[2] NIYATO D., HOSSAIN E.: 'Spectrum trading in cognitive radio networks: a market-equilibrium-based approach', *IEEE Wirel. Commun.*, 2008, **15**, (6), pp. 71–80

[3] ENGHETA N., ZIOLKOWSKI R.W.: 'Metamaterials physics and engineering explorations' (John Wiley & Sons, Inc., 2006, 1st edn.)

[4] CALOZ C., ITOH T.: 'Electromagnetic metamaterials transmission line theory and microwave applications' (John Wiley & Sons, Inc., 2006, 1st edn.)

[5] YABLONOVITCH E.: 'Photonic band-gap structures', *J. Opt. Soc. of Am.*, 1993, **10**, (2), pp. 283–295

[6] YABLONOVITCH E.: 'Inhibited spontaneous emission in solid-state physics and electronics', *Phys. Rev. Lett.*, 1987, **58**, (20), pp. 2059–2062

[7] FEI-RAN Y., KUANG-PING M., YONGXI Q., ITOH T.: 'A uniplanar compact photonic-bandgap (UC-PBG) structure and its applications for microwave circuit', *IEEE Trans. Microw. Theory and Tech.*, 1999, **47**, (8), pp. 1509–1514

[8] OZBAY E., AYDIN K., BUTUN S., KOLODZIEJAK K., PAWLAK D.: 'Ferroelectric based tuneable SRR based metamaterial for microwave applications'. 37th European Microwave Conf., October 2007, pp. 497–499

[9] VELEZ A., BONACHE J., MARTIN F.: 'Varactor-loaded complementary split ring resonators (VLCSRR) and their application to tunable metamaterial transmission lines', *IEEE Microw. Wirel. Compon. Lett.*, 2008, **18**, (1), pp. 28–30

[10] KUYLENSTIERNA D., ASH E., VOROBIEV A., ITOH T., GEVORGIAN S.: 'X-band left handed phase shifter using thin film $Ba_{0.25}SR_{0.75}TiO_3$ Ferroelectric Varactors'. 36th European Microwave Conf., September 2006, pp. 847–850

[11] ABDALLA M.A.Y., PHANG K., ELEFTHERIADES G.V.: 'Printed and integrated CMOS positive/negative refractive-index phase shifters using tunable active inductors', *IEEE Trans. on Microw. Theory Tech.*, 2007, **55**, (8), pp. 1611–1623

[12] HOLLOWAY C.L., KUESTER E.F., BAKER-JARVIS J., KABOS P., MOHAMED M.: 'Double negative (DNG) index composite structure from non-conducting materials with an application to controllable surfaces'. Conf. on Electrical Insulation and Dielectric Phenomena, CEIDP'04, 2004 Annual Report, October 2004, pp. 143–144

[13] HAND T., CUMMER S.: 'Characterization of tunable metamaterial elements using MEMS switches', *IEEE Antennas Wirel. Propag. Lett.*, 2007, **6**, pp. 401–404

[14] DEGIRON A., MOCK J.J., SMITH D.R.: 'Optical control of metamaterial unit cells at microwave frequencies', Int. Symp. on Signals, Systems and Electronics, ISSSE'07,2007, pp. 209–212

[15] MERCIER L., RODES E., DROUET J., *ET AL.*: 'Steerable and tunable "EBG resonator antennas" using smart metamaterials'. IEEE Antennas and Propagation Society Int. Symp. 2006, pp, 406–409

[16] BOSSARD J.A., LIANG X., LI L., *ET AL.*: 'Tunable frequency selective surfaces and negative-zero-positive index metamaterials based on liquid crystals', *IEEE Trans. Antennas Propag.*, 2008, **56**, (5), pp. 1308–1320

[17] BRILLOUIN L.: 'Wave propagation in periodic structures: electric filters and crystal lattices' (McGraw-Hill, New York, 1946)

[18] ZHANG L., ALEXOPOULOS N.G., SIEVENPIPER D., YABLONOVITCH E.: 'An efficient finite-element method for the analysis of photonic band-gap materials', *IEEE MTT-S Int. Microw. Symp. Dig.*, 1999, **4**, pp. 1703–1706

[19] COCCIOLI R., YANG F.R., MA K.P., ITOH T.: 'Aperture-coupled patch antenna on UCPBG substrate', *IEEE Trans. Microw. Theory Tech.*, 1999, **47**, (11), pp. 2123–2130

[20] ZHOU Y., LUCYSZYN S.: 'HFSS™ modelling anomalies with THz metal-pipe rectangular waveguide structures at room temperature', *PIERS Online*, 2009, **5**, (3), pp. 201–211

[21] HERBERTZ K., LUCYSZYN S.: 'Two-dimensional metamaterials for dual-band filter applications'. 38th European Microwave Conf., October 2008, pp. 1366–1369

[22] LUCYSZYN S., ROBERTSON I.D.: 'Decade bandwidth hybrid analogue phase shifter using MMIC reflection terminations', *IEE Electron. Lett.*, 1992, **28**, (11), pp. 1064–1065

[23] LUCYSZYN S., GREEN G., ROBERTSON I.D.: 'Accurate millimeter-wave large signal modeling of planar Schottky varactor diodes'. IEEE MTT-S Symp. on Digest, Albuquerque, USA, June 1992, pp. 259–262

[24] LUCYSZYN S., GREEN G., ROBERTSON I.D.: 'Interdigitated planar Schottky varactor diodes for tunable MMIC applications'. Proc. ESA/IEEE European Gallium Arsenide Applications Symp., (GAAS'92), ESTEC, Noordwijk, The Netherlands, Session 1B, April 1992

[25] LUCYSZYN S., LUCK J., GREEN G., ROBERTSON I.D.: 'Enhanced modelling of interdigitated planar Schottky varactor diodes'. IEEE Asia-Pacific Microwave Conf., (APMC'92), Adelaide, Australia, August 1992, pp. 273–278

[26] LUCYSZYN S., ROBERTSON I.D.: 'Optically-induced measurement anomalies with voltage-tunable analog control MMICs', *IEEE Trans. Microw. Theory Tech.*, 1998, **46**, (8), pp. 1105–1114